Unconventional order/disorder behaviour in Al–Co–Cu–Fe–Ni multi-principal element alloys after casting and annealing

P. Priputen [a,*], P. Noga [b], M. Novaković [c], J. Potočnik [c], A. Antušek [b], R. Bujdák [b], E. Bachleda [a], M. Drienovský [a], M. Nosko [d]

[a] Slovak University of Technology in Bratislava, Faculty of Materials Science and Technology in Trnava, Institute of Materials Science, J. Bottu 25, 917 24, Trnava, Slovakia
[b] Slovak University of Technology in Bratislava, Faculty of Materials Science and Technology in Trnava, Advanced Technologies Research Institute, J. Bottu 25, 917 24, Trnava, Slovakia
[c] Department of Atomic Physics, Vinča Institute of Nuclear Sciences - National Institute of the Republic of Serbia, University of Belgrade, Belgrade, Serbia
[d] Institute of Materials and Machine Mechanics, Slovak Academy of Sciences, Dúbravská cesta 9, 845 13, Bratislava, Slovakia

A B S T R A C T

The effect of Cu concentration on the order/disorder behaviour of the $AlCoCu_xFeNi$ ($x = 0.6$ to 3.0) multi-principal element alloys was investigated. BCC and/or FCC phases were observed in the microstructures of the alloys after casting and annealing at 1050 °C followed by slow cooling. Interesting is that the alloys form ordered structures after casting and disordered structures after annealing and slow cooling, while the opposite would be expected. The ordering in the as-cast state is explained by the strong affinity of Al to transition metals, which results in the formation of supercell structures having sublattices occupied by certain elements only. Disordering after annealing has two reasons. Either the phase is composed of nearly pure element (Cu) and is disordered by default or it is composed of randomly distributed nano-segregated regions within a single phase resulting in a uniform distribution of all elements in the sublattices and therefore appearing to be macroscopically disordered. The reason for the formation of such nano-segregated areas might reside in the reduction of Gibbs free energy due to the annealing by the interplay between enthalpy and entropy.

1. Introduction

Multi-principal element alloys (MPEAs) – a new class of alloys, containing more than only one or two basic elements as in the case of conventional alloys, brought a new paradigm to metallurgy and opened a very active field of research [1–3]. The large combinatorial space of MPEAs [4] is very attractive and promises new alloys with highly interesting properties and application potential to be discovered [5–10]. The most pronounced property of MPEAs is that the number of coexisting phases in these alloys stays small even for a large number of elements, and solid solutions with FCC, BCC or HCP lattice are usually formed. Initially, it was assumed that the stabilization of solid solutions at the expense of intermetallics arises from a reduction of free Gibbs energy by high configurational entropy due to a large number of elements randomly distributed in the lattice, which also coined their original name – high-entropy alloys (HEAs) [11,12]. However, as it was found later [1,4,13–15], in addition to the high-entropy effect, enthalpy plays an important role as well and both need to be taken into account in phase prediction and alloy design. Furthermore, many reports have shown that some observed HEAs are not genuinely single-phase alloys as

was originally assumed in the HEAs concept [4,13–21].

It is supposed that the high-entropy effect is manifested mainly at high temperatures, allowing the formation of disordered solid solutions after casting. On the other hand, annealing increases the probability of producing intermetallics or ordered solid solutions [4,22]. However, in the equiatomic AlCoFeNi alloy, an interesting behaviour has been reported [23]. The alloy consists of a single BCC phase which is ordered in the as-cast state, while after annealing and slow cooling, it changes from ordered to disordered which is the opposite of what would be expected. This raises a few questions: What is the reason for such behaviour? Would the same effect manifest itself when the structure changed from BCC to FCC, which is also often observed in MPEAs? This work aims to try to provide answers to the above questions. Cu is considered to be a typical FCC stabilizing element [4], therefore, a gradual change of the structure from BCC to FCC is expected by the addition of Cu to the AlCoFeNi alloy, which allows investigating this change and the effect of Cu content on the order/disorder behaviour of the phases formed after casting as well as after annealing and slow cooling.

Table 1

Calculated enthalpy of formation for binary systems combining Al, Ni, Fe, Co, Cu elements in BCC lattice.

Binary system	Enthalpy of formation [kJ/mol]
Al–Ni	−63.619
Al–Fe	−25.814
Al–Co	−55.249
Al–Cu	−11.623
Ni–Fe	4.785
Ni–Co	14.628
Ni–Cu	9.577
Fe–Co	−9.132
Fe–Cu	25.689
Co–Cu	28.452

2. Experimental and theoretical methods

Six AlCoCu$_x$FeNi alloys with various ratios of Cu ($x = 0.6, 1.0, 1.5, 2.0, 2.5, 3.0$) were prepared from high-purity elements (>99.99 wt%) by arc-melting under an argon atmosphere. The samples were re-melted five times to obtain a homogeneous chemical composition of the alloys. After the final re-melting, the alloys were cast into cylinder-shaped samples by the suction casting method and their microstructure was analyzed. After analysis, samples were annealed at 1050 °C for one day followed by slow cooling down to room temperature at the rate of 5 °C/h. Subsequently, the microstructure of the samples was analyzed again. For the annealing experiment, the samples were placed in small alumina crucibles, which were enclosed into silica glass tubes, purged several times with argon and sealed at 1 bar pressure. Alumina crucibles were used to prevent direct contact of the samples with silica during the annealing experiment to avoid possible contamination with silicon.

A PANalytical Empyrean x-ray diffractometer and a JEOL JSM-7600F scanning electron microscope (SEM) equipped with an Oxford instruments X-MAX energy dispersive x-ray spectrometer (EDX) using the INCA software were used to characterize the microstructure of the as-cast and annealed alloys. All images were taken in BSE mode. X-ray diffraction experiments (XRD) were carried out on both powder and bulk samples with the nickel filtered Cu-K$_\alpha$ radiation, between 20° and 100° of 2θ with a 0.02° step. The chemical composition of the observed phases was determined by EDX.

Phase morphology and ordering of individual phases in the microstructures were investigated on selected samples by (high-resolution) transmission electron microscopy (HRTEM/TEM), using an FEI Talos F200X TEM, equipped with a CCD camera with a resolution of 4096 × 4096. The micrographs were taken at 200 kV acceleration voltage. TEM-
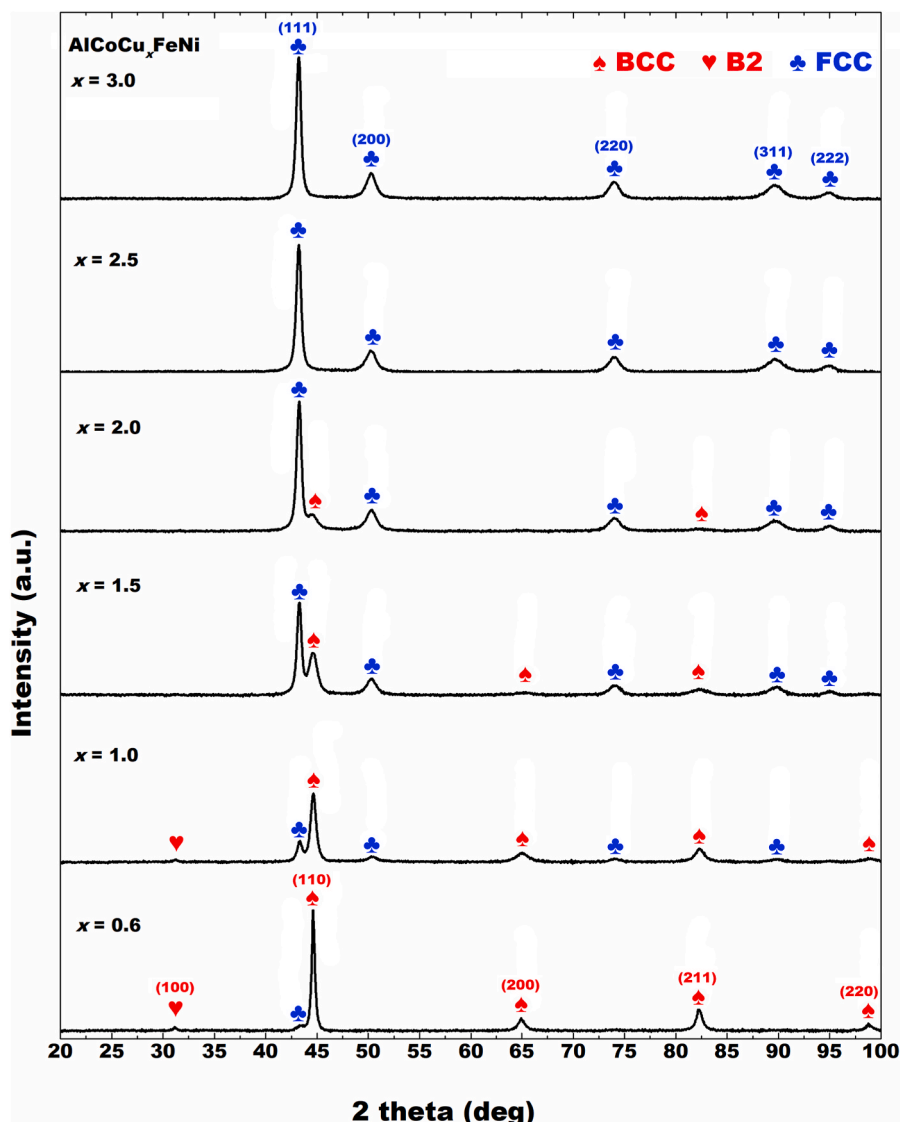

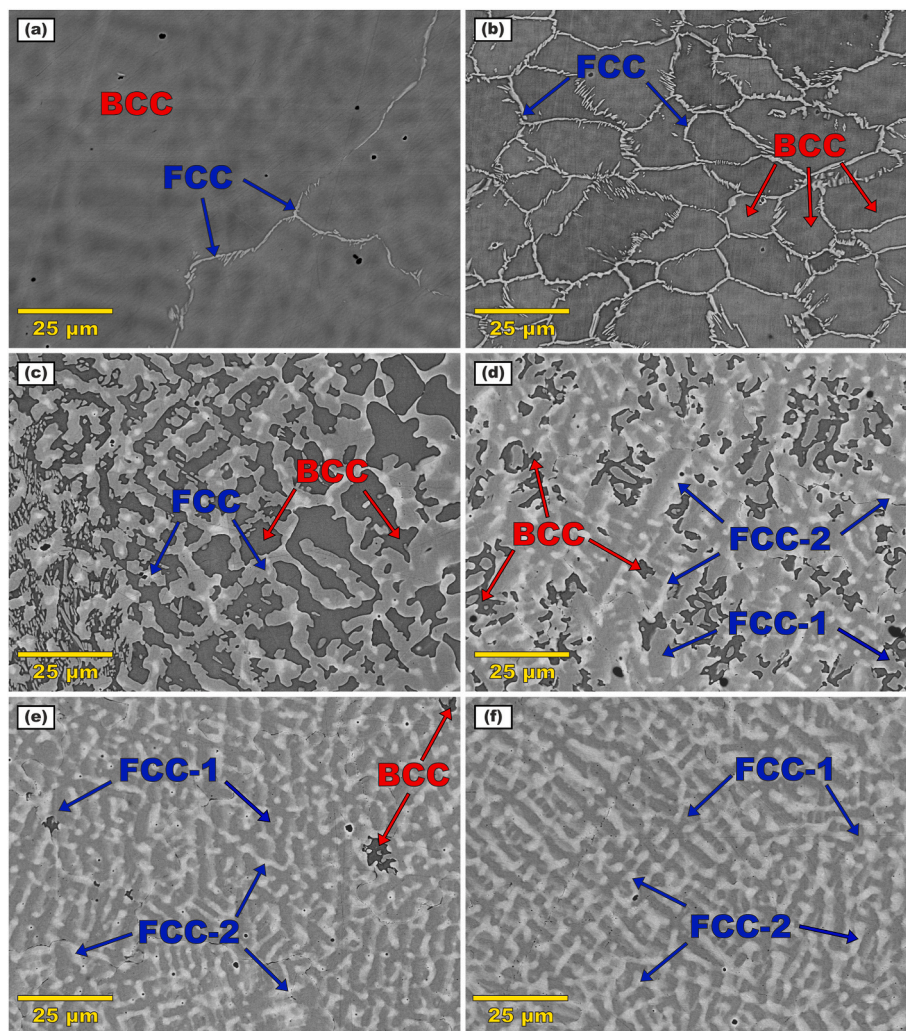**Fig. 1.** Powder XRD records of AlCoCu$_x$FeNi ($x = 0.6, 1.0, 1.5, 2.0, 2.5, 3.0$) alloys in the as-cast state.

Fig. 2. As-cast microstructures of AlCoCu$_x$FeNi alloys with various Cu contents: (a) $x = 0.6$, (b) $x = 1.0$, (c) $x = 1.5$, (d) $x = 2.0$, (e) $x = 2.5$, (f) $x = 3.0$.

EDX in scanning transmission (STEM) mode was used for element colour mapping. High-angle annular dark-field (HAADF) images were captured in nanoprobe-TEM mode with probes of below 1 nm size and a camera length of ~200 mm. The crystal structure of different sample regions was determined using selected-area electron diffraction (SAED) and fast Fourier transform (FFT) analysis. The samples were examined in cross-section, and TEM lamellae were prepared using FIB (FEI Scios2 Dual Beam System) and set onto a copper grid.

To analyze the effect of enthalpy on the atomic configuration of the BCC phases, Monte Carlo (MC) simulations [24] for a fixed BCC lattice (modelled with periodic boundary conditions) were performed using the Bragg-Williams model with pair interaction energies between the nearest-neighbour atoms [25]. Pair interaction energies were based on binary formation enthalpies H_{ij} calculated for BCC lattice (Table 1). Binary formation enthalpies H_{ij} were calculated by the DFT method using Perdew-Burke-Ernzerhof functional [26] and corresponding Vanderbilt ultrasoft pseudopotentials [27] with 80Ry energy cutoff for wavefunctions and with k-space sampling 10x10x10. Spin-polarized calculations were used for alloys containing ferromagnetic elements of Fe, Co, and Ni.

The pair interaction energies have been derived as follows [28]:

$$v_{ij} = H_{ij}/z \qquad (1)$$

where $z = 8$ is the coordination number for the BCC structure.

In the MC simulations, the energy change ΔE corresponding to the interchange of two randomly selected atoms was evaluated and the exchange was accepted or rejected using the Metropolis algorithm [29], i.e. if the random number uniformly generated from the [0,1] interval was larger than the Boltzmann factor

$$\exp(-\Delta E / k_B T) \qquad (2)$$

the exchange of atoms was accepted, otherwise, the exchange was rejected. (k_B is the Boltzmann constant and T is temperature).

3. Results and discussion

3.1. Microstructure and phase analysis of as-cast alloys

XRD records of as-cast AlCoCu$_x$FeNi alloys with various ratios of copper ($x = 0.6, 1.0, 1.5, 2.0, 2.5, 3.0$) are shown in Fig. 1. Two phases with BCC and FCC lattices in different ratios depending on the amount of copper in the alloys were identified from the records. In the record of the AlCoCu$_{0.6}$FeNi alloy, all peaks of the BCC phase are observed along with a weak (111) FCC peak, so the AlCoCu$_{0.6}$FeNi alloy is almost entirely composed of the BCC phase. With increasing Cu content, peaks of the FCC phase increase at the expense of the BCC peaks. Finally, the AlCoCu$_{2.5}$FeNi and AlCoCu$_{3.0}$FeNi alloys records correspond completely to the FCC phase. Minor (100) superlattice reflection at ~32° observed in AlCoCu$_{0.6}$FeNi and AlCoCu$_{1.0}$FeNi alloys indicates that the BCC phase is ordered.

Table 2
Chemical composition (at. %) of as-cast and annealed AlCoCu$_x$FeNi alloys and their phases measured by SEM-EDX.

Copper content	State	Area	Chemical composition (at.%)					Identified phases
			Al	Co	Cu	Fe	Ni	
$x = 0.6$	As-cast	**Overall**	**21.8**	**21.8**	**12.8**	**21.9**	**21.7**	
		Dark + light	21.7 ± 0.3	21.8 ± 0.3	12.6 ± 0.4	22.2 ± 0.1	21.7 ± 0.1	BCC + FCC
	Annealed	**Overall**	**21.8**	**21.9**	**12.2**	**22.1**	**22.0**	
		Dark grey	27.0 ± 0.1	22.8 ± 0.1	5.0 ± 0.2	21.4 ± 0.2	23.7 ± 0.1	BCC
		Light grey	8.0 ± 0.2	18.0 ± 0.3	36.4 ± 2.0	24.6 ± 1.1	13.0 ± 0.3	Mixed region
$x = 1.0$	As-cast	**Overall**	**20.5**	**20.2**	**19.1**	**20.3**	**19.9**	
		Dark grey	21.3 ± 0.4	22.5 ± 0.5	13.4 ± 1.1	22.5 ± 0.3	20.3 ± 0.2	BCC
		Light grey	14.1 ± 0.8	7.8 ± 2.4	58.0 ± 8.4	7.8 ± 2.7	12.3 ± 2.7	FCC
	Annealed	**Overall**	**21.0**	**20.1**	**18.5**	**20.1**	**20.3**	
		Dark grey	27.4 ± 0.2	22.6 ± 0.1	5.1 ± 0.1	20.7 ± 0.1	24.1 ± 0.2	BCC
		Light grey	7.4 ± 0.2	14.6 ± 0.1	47.3 ± 0.7	18.3 ± 0.2	12.4 ± 0.2	Mixed region
$x = 1.5$	As-cast	**Overall**	**19.2**	**18.3**	**25.9**	**18.4**	**18.2**	
		Dark grey	22.1 ± 0.9	20.1 ± 0.3	19.2 ± 1.0	20.2 ± 0.8	18.4 ± 0.6	BCC
		Light grey	15.8 ± 0.6	13.8 ± 2.9	40.6 ± 8.0	14.1 ± 3.2	15.7 ± 1.8	FCC
	Annealed	**Overall**	**20.5**	**18.1**	**25.0**	**18.2**	**18.2**	
		Dark grey	26.0 ± 0.1	23.7 ± 0.1	5.3 ± 0.1	21.6 ± 0.2	23.4 ± 0.2	BCC
		Light grey	6.7 ± 0.2	12.3 ± 0.1	54.8 ± 0.5	16.1 ± 0.2	10.1 ± 0.1	Mixed region
$x = 2.0$	As-cast	**Overall**	**17.3**	**16.9**	**31.8**	**17.1**	**16.9**	
		Dark grey	26.0 ± 1.2	16.8 ± 1.2	21.9 ± 1.7	14.7 ± 1.8	20.6 ± 0.4	BCC
		Light grey	13.7 ± 0.2	24.8 ± 0.3	17.6 ± 0.3	26.9 ± 0.3	17.0 ± 0.1	FCC-1
		White	15.8 ± 0.7	4.8 ± 1.0	66.0 ± 4.0	4.3 ± 1.0	9.1 ± 1.4	FCC-2
	Annealed	**Overall**	**18.8**	**16.8**	**30.5**	**16.9**	**17.0**	
		Dark grey	28.1 ± 0.1	23.3 ± 0.1	5.2 ± 0.1	21.0 ± 0.1	22.4 ± 0.1	BCC
		Light grey	7.4 ± 0.2	11.2 ± 0.4	57.8 ± 1.2	14.2 ± 0.6	9.4 ± 0.4	Mixed region
$x = 2.5$	As-cast	**Overall**	**15.8**	**15.5**	**37.5**	**15.6**	**15.6**	
		Dark grey	25.6 ± 0.8	16.6 ± 0.8	23.5 ± 0.1	14.7 ± 1.6	19.6 ± 1.4	BCC
		Light grey	15.1 ± 0.4	21.7 ± 0.5	23.6 ± 0.9	22.5 ± 0.8	17.1 ± 0.2	FCC-1
		White	15.3 ± 0.4	7.1 ± 0.6	60.5 ± 2.4	6.5 ± 0.8	10.6 ± 0.8	FCC-2
	Annealed	**Overall**	**17.1**	**15.7**	**35.6**	**15.6**	**16.0**	
		Dark grey	27.2 ± 0.1	23.9 ± 0.1	5.1 ± 0.1	20.9 ± 0.1	22.9 ± 0.1	BCC
		Light grey	7.5 ± 0.4	10.9 ± 0.2	58.7 ± 0.9	13.4 ± 0.2	9.6 ± 0.2	Mixed region
$x = 3.0$	As-cast	**Overall**	**15.0**	**14.3**	**41.5**	**14.8**	**14.4**	
		Light grey	12.1 ± 0.2	24.6 ± 0.1	20.4 ± 0.2	26.9 ± 0.3	16.0 ± 0.1	FCC-1
		White	15.5 ± 0.2	3.6 ± 0.5	70.1 ± 2.1	3.1 ± 0.4	7.7 ± 1.1	FCC-2
	Annealed	**Overall**	**17.0**	**14.3**	**39.4**	**14.8**	**14.5**	
		Dark grey	27.1 ± 0.1	24.1 ± 0.1	5.4 ± 0.1	20.8 ± 0.2	22.6 ± 0.1	BCC
		Light grey	7.6 ± 0.4	10.1 ± 0.3	60.9 ± 0.8	12.2 ± 0.4	9.4 ± 0.2	Mixed region

Thus, as expected, in the as-cast AlCoCu$_x$FeNi alloys ($x = 0.6$, 1.0, 1.5, 2.0, 2.5, 3.0) the gradual change of Cu-content leads to the gradual change of alloys structure from BCC to FCC.

However, without a microstructure study, this information is incomplete. As was reported in Refs. [4,13,14], many high-entropy alloys in the earlier studies were wrongly identified as single-phase alloys based on XRD analysis only. A closer look at the microstructures of investigated alloys reveals more interesting details.

As-cast microstructures of AlCoCu$_x$FeNi alloys with various ratios of copper ($x = 0.6$, 1.0, 1.5, 2.0, 2.5, 3.0) are shown in Fig. 2. All alloys exhibit a typical casting microstructure with dendritic (DR) and interdendritic (ID) morphology. Chemical compositions of alloys, as well as their constituents, are listed in Table 2. The microstructure of AlCoCu$_{0.6}$FeNi alloy (Fig. 2a) is almost entirely composed of one constituent
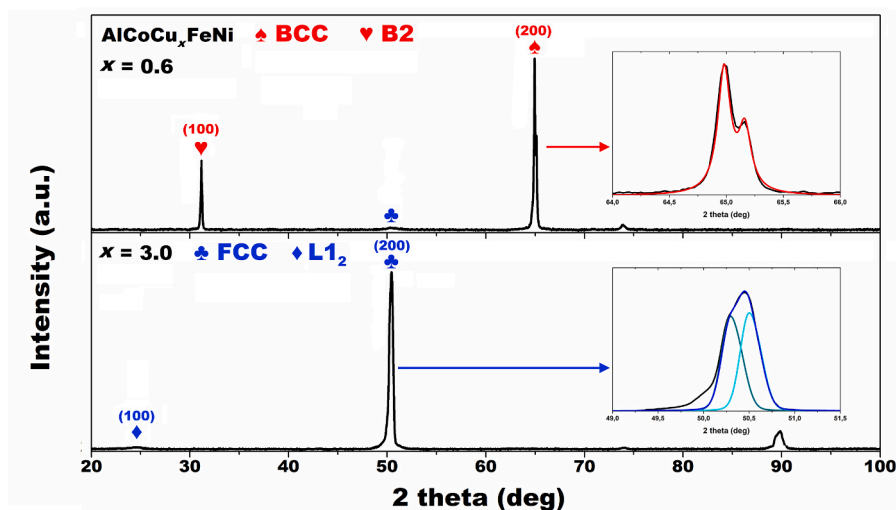

Fig. 3. Bulk XRD records of AlCoCu$_x$FeNi ($x = 0.6$ and $x = 3.0$) alloys. The insets present details of the measured and fitted BCC-(200) and FCC-(200) peaks for AlCoCu$_x$FeNi ($x = 0.6$ and $x = 3.0$) alloys, respectively.
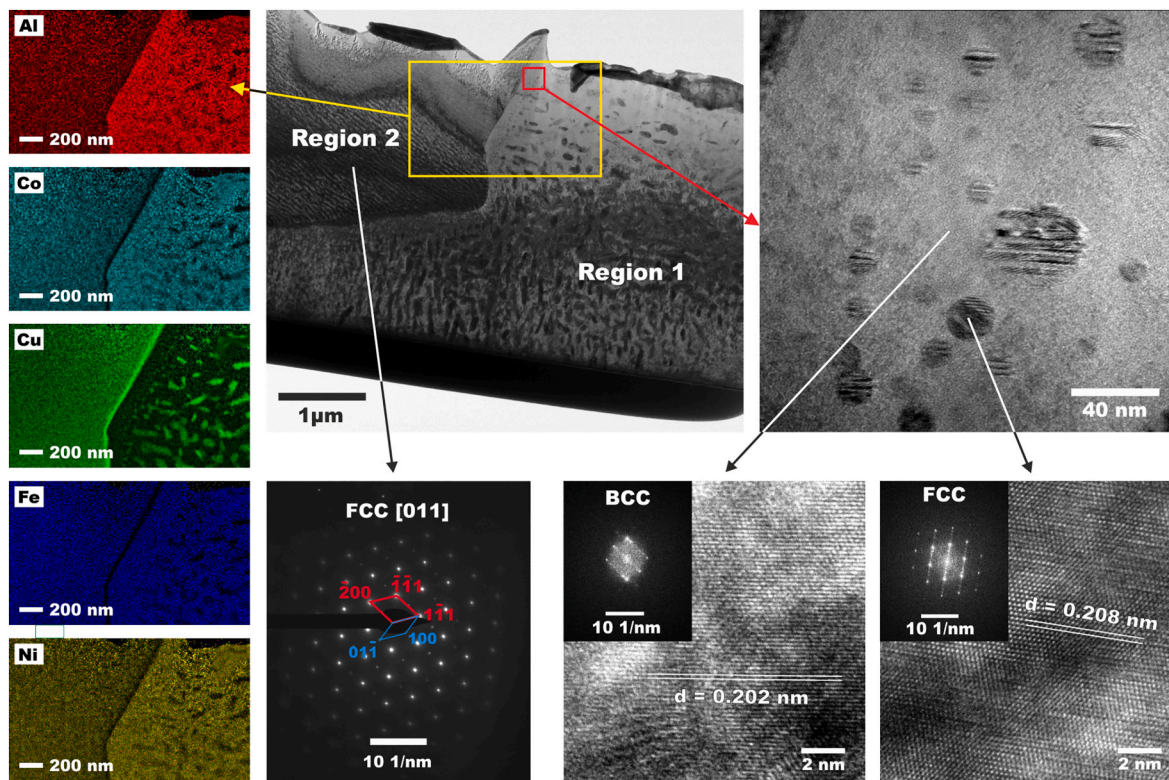
Fig. 4. TEM analysis of the AlCoCu$_{1.5}$FeNi alloy: top middle – TEM bright-field micrograph; bottom middle – SAED pattern of region 2; left – EDX mapping of the yellow highlighted area; top right – detail on the FCC Cu nanoparticles in the BCC matrix from the red highlighted area; bottom right – HRTEM images of the FCC Cu nanoparticle and the BCC matrix with the corresponding FFT patterns.

corresponding to the BCC phase, as follows from the XRD record. The FCC phase was found only at the grain boundaries in trace amounts. With increasing Cu content, ID light grey areas of the FCC phase grow at the expense of DR dark grey areas of the BCC phase, occurring also within the BCC phase in addition to grain boundaries. The results obtained for the equiatomic AlCoCuFeNi alloy are in agreement with those reported in Refs. [30,31]. At $x = 2.0$ (Fig. 2d) the FCC phase becomes dominant and appears in the form of DR light grey areas (FCC−1) as well as white Cu-rich ID areas (FCC−2). Further, for the case of $x = 2.5$ (Fig. 2e), the amount of the BCC phase is extremely small and its peaks are not observable anymore in the corresponding XRD record. Finally, the AlCoCu$_{3.0}$FeNi alloy (Fig. 2f) consists only of two FCC phases: AlCoCuFeNi solid solution enriched by Fe–Co with respect to the alloy composition (FCC−1) and Cu-rich solid solution (FCC−2). Both forms are probably already present in the alloys for $x = 0.6$–1.5, which can be deduced from the unusually large standard deviations of the Cu stoichiometry in the FCC phase. The obtained results are similar to those reported in Ref. [32] for AlCrFeCoNiCu$_x$ alloys ($x = 0, 0.5, 1.0, 2.0, 3.0$). Both FCC phases were also observed previously in the Fe–Ni–Co–Cu system at high temperatures [33].

Thus, the FCC phase, which appeared to be a single-phase from the XRD experiments, actually consists (at least at higher Cu concentrations) of two FCC phases, with different compositions. To determine the lattice parameters of all found phases, XRD experiments on bulk samples were performed to exclude possible stresses induced during the powderization process which could cause a peak broadening in diffraction records of powder samples. Records for terminal cases ($x = 0.6$ and $x = 3.0$) are shown in Fig. 3. In both alloys, a predominant $\langle k00 \rangle$ orientation was observed for both phases, as was also reported in Refs. [34,35]. The highest peak analysis in the records showed that the (200) peak of the BCC phase is a single Kα_1/Kα_2 peak ($a_{BCC} = 2,869$ Å), while the (200) peak of the FCC phase consists actually of two very close Kα_1/Kα_2 peaks (see insets in Fig. 3) corresponding to two FCC phases with very close lattice parameters ($a_{FCC-1} = 3.615$ Å, $a_{FCC-2} = 3.629$ Å). Superlattice reflections (100), typical for the ordered structure, can also be found in the records of both phases, particularly for the BCC phase, indicating that the phases are ordered to some extent, similar to the AlCoFeNi system [23].

To investigate the morphology of the phases in more detail, especially the eventual coexistence of ordered and disordered BCC phases

Table 3
Chemical composition (at. %) of phases in selected as-cast and annealed AlCoCu$_x$FeNi alloys measured by TEM-EDX.

| Copper content	State	Area	Chemical composition (at.%)					Identified phases
			Al	Co	Cu	Fe	Ni	
$x = 1.5$	As-cast	Region 1	22.0 ± 2.2	21.6 ± 3.6	20.0 ± 3.3	16.9 ± 2.8	19.4 ± 3.2	BCC + FCC particles
		Particle	4.7 ± 2.1	1.8 ± 1.2	89.5 ± 22.9	1.2 ± 1.1	2.8 ± 1.3	FCC
		Region 2	13.5 ± 1.5	18.5 ± 3.2	33.7 ± 5.9	18.6 ± 3.2	15.7 ± 2.7	FCC
	Annealed	Region 1	22.6 ± 2.3	23.5 ± 3.9	11.8 ± 2.0	21.0 ± 3.5	21.1 ± 3.5	BCC
		Region 2	2.2 ± 0.5	0.6 ± 0.2	93.4 ± 23.9	0.6 ± 0.2	3.2 ± 0.8	FCC
		Region 3	4.3 ± 0.5	25.8 ± 4.6	19.3 ± 3.4	37.4 ± 6.7	13.2 ± 2.4	BCC
$x = 3.0$	As-cast	Region 1	8.8 ± 1.0	20.3 ± 3.6	36.8 ± 6.5	20.0 ± 3.6	14.1 ± 2.5	FCC-1
		Region 2	8.2 ± 1.5	3.9 ± 0.9	78.0 ± 18.0	3.5 ± 0.8	6.4 ± 1.5	FCC-2
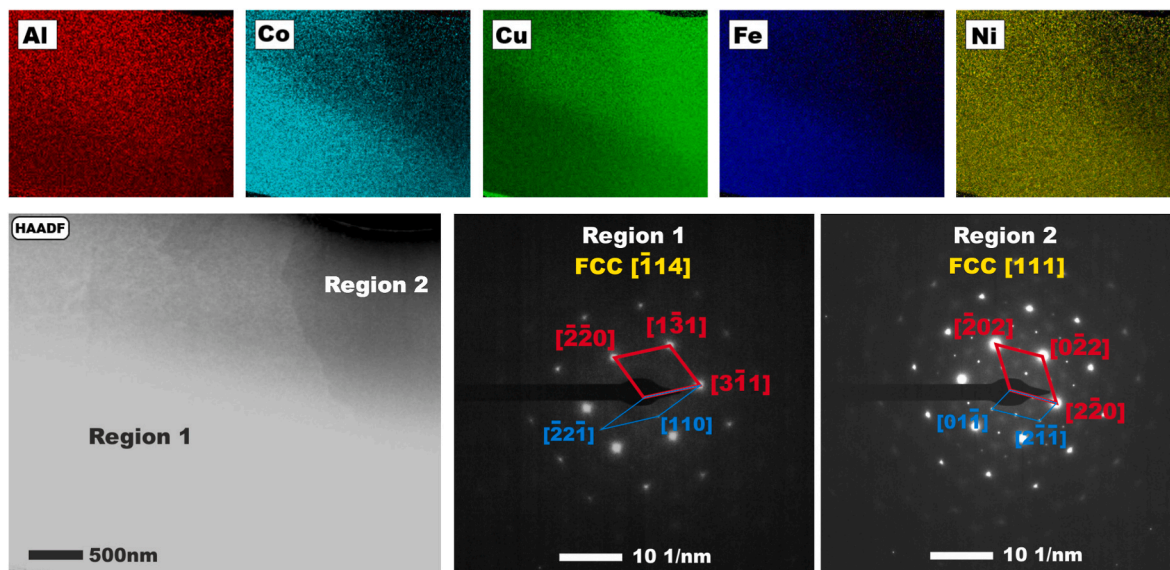
Fig. 5. TEM analysis of the AlCoCu$_{3.0}$FeNi alloy: top – EDX mapping; bottom left – HAADF image recorded in STEM mode, where two distinct regions are observable; bottom right - SAED patterns of both regions.
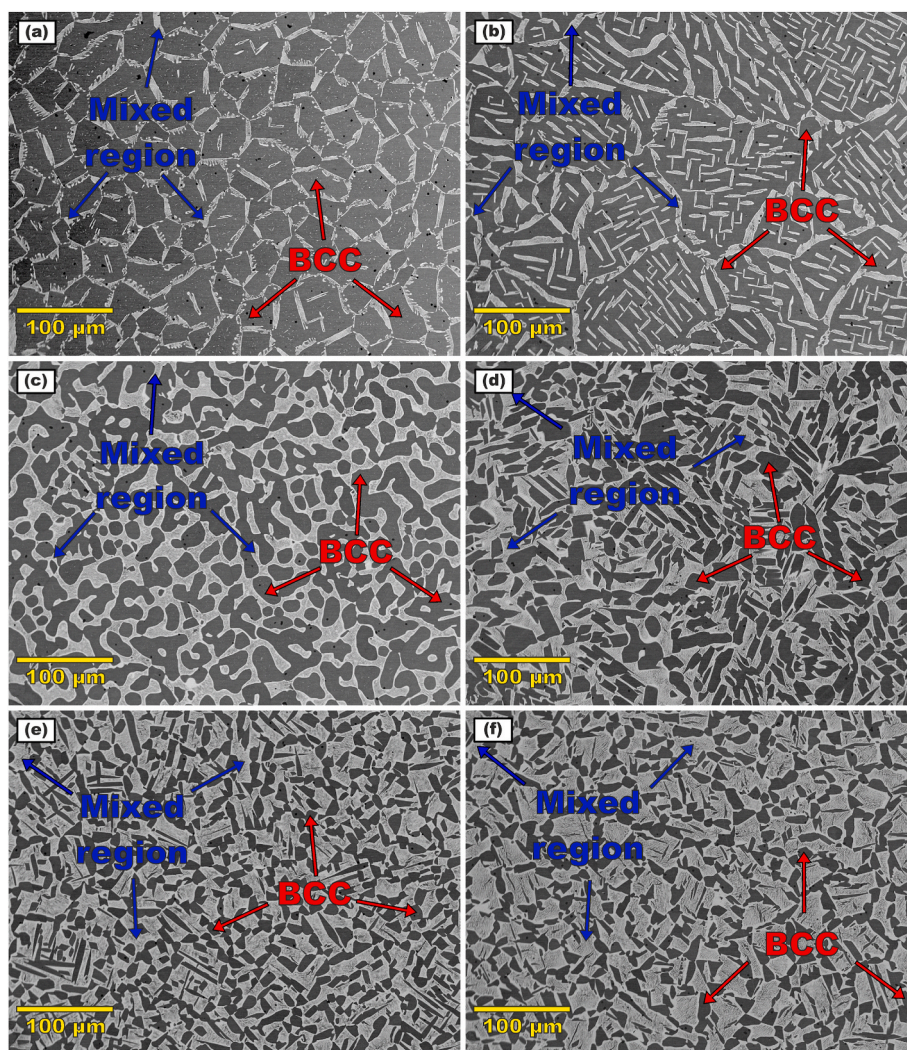

Fig. 6. Microstructures of AlCoCu$_x$FeNi alloys with various Cu contents after annealing at 1050 °C followed by slow cooling: (a) $x = 0.6$, (b) $x = 1.0$, (c) $x = 1.5$, (d) $x = 2.0$, (e) $x = 2.5$, (f) $x = 3.0$.
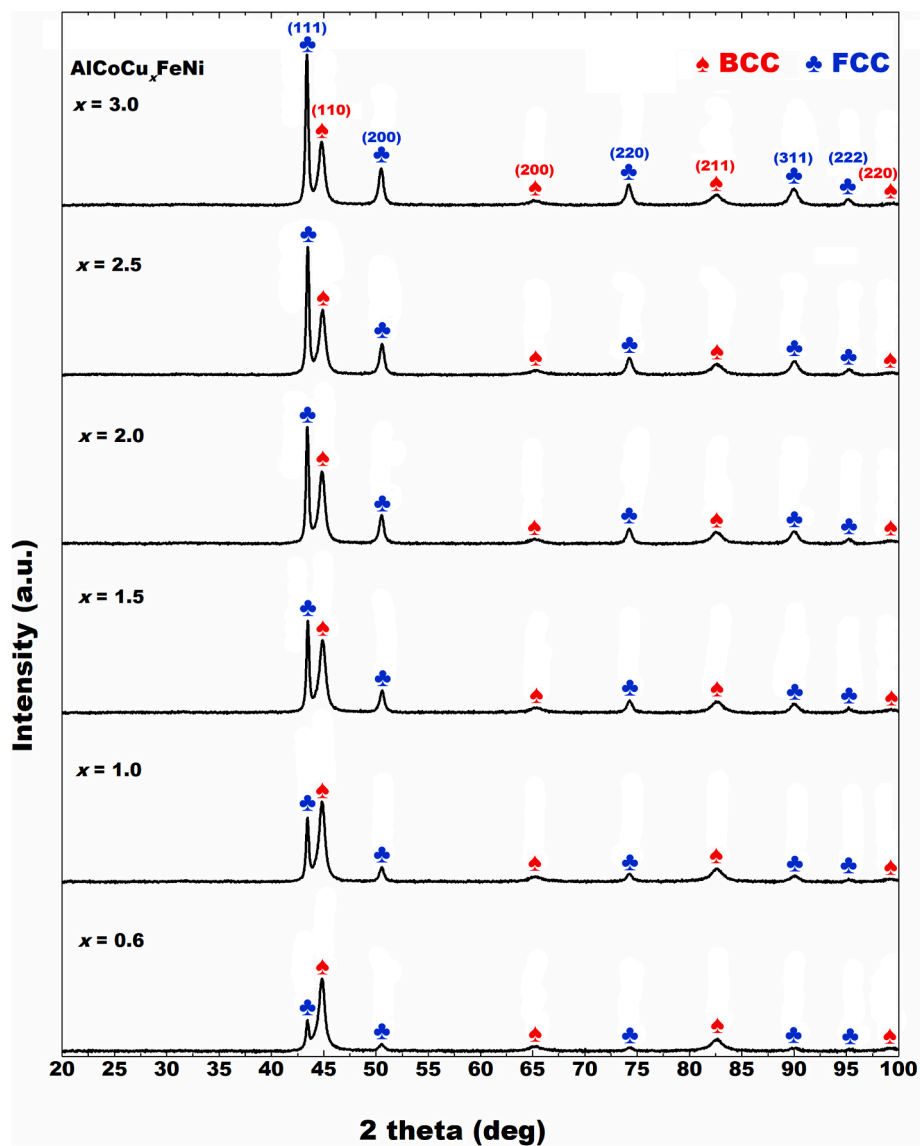
Fig. 7. Powder XRD records of AlCoCu$_x$FeNi (x = 0.6, 1.0, 1.5, 2.0, 2.5, 3.0) alloys after annealing at 1050 °C followed by slow cooling.

[36–38], as well as the ordering of the FCC phases, the AlCoCu$_{1.5}$FeNi alloy (approximately the same amount of BCC and FCC phases) and the AlCoCu$_{3.0}$FeNi alloy (only FCC−1 and FCC−2 phases) were studied by HRTEM. Results obtained for the AlCoCu$_{1.5}$FeNi alloy are summarized in Fig. 4. From the low magnification TEM bright-field micrograph, two different regions (phases) separated by a grain boundary are observed. The chemical composition of both regions is listed in Table 3. The compositions match well with those in Table 2 for AlCoCu$_{1.5}$FeNi alloy and respective phases. The analysis of the yellow highlighted area shows that region 1 consists of a BCC matrix with Cu-rich FCC particles, and region 2 has a homogenous FCC structure. The coexistence of ordered and disordered BCC phases in region 1 was not detected. While the FCC structure of region 2 was confirmed by SAED, the structure of region 1 and the Cu-rich particles was determined by FFT only, as due to the particles present in the BCC matrix did not enable reliable SAED analysis. The presence of Cu-rich particles in the BCC structure probably contributes to a higher concentration of Cu in the chemical composition of the BCC phase (Tables 2 and 3). In the SAED from region 2, apart from the strong reflections (red), weak superlattice reflections (blue) are also observed, confirming that the FCC phase is ordered. A high magnification TEM bright-field micrograph of the red highlighted area shows the morphology of region 1 in detail, where the presence of Cu-rich FCC

particles inside the BCC matrix is clearly visible. Similar nano-twinned FCC precipitates were also observed in the AlCoCuFeNi alloy reported in Ref. [39].

The HAADF image (recorded in STEM mode) of the AlCoCu$_{3.0}$FeNi alloy with corresponding STEM-EDX maps and SAED patterns is shown in Fig. 5, where two regions can be observed. In both regions, FCC−1 as well as FCC−2, the ordered FCC structure is also confirmed. The composition of the FCC−2 region (Table 3) shows the Cu-rich phase, in correspondence with SEM observations. Deviation in the compositions using SEM-EDX and TEM-EDX techniques results from the fact that the phases after casting are not homogeneous but variation in the composition can be observed within the phase. Thus, the composition is different in the middle of the phase, usually analyzed by SEM-EDX, than close to the phase boundary, analyzed by TEM-EDX.

3.2. Microstructure and phase analysis of annealed alloys

Based on differential thermal analysis, the investigated alloys were subjected to an annealing process at a temperature below the solidification temperature which was set to 1050 °C. Microstructures of the investigated alloys after annealing at 1050 °C followed by slow cooling are shown in Fig. 6. The microstructure of the samples changed from fine
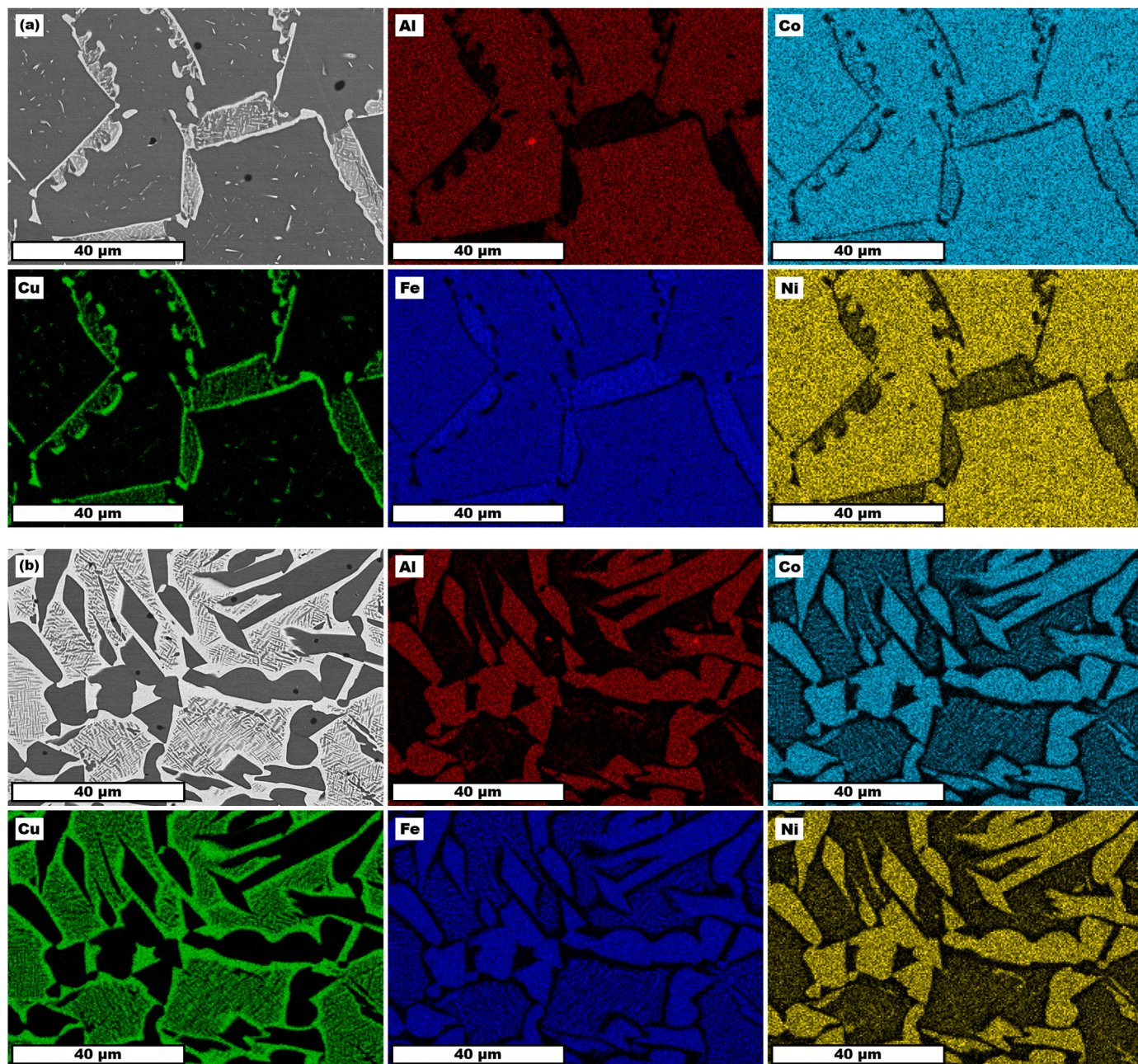
Fig. 8. Relative EDX mapping of AlCoCu$_x$FeNi alloys after annealing at 1050 °C followed by slow cooling: (a) ($x = 0.6$), (b) ($x = 3.0$).

dendritic to coarse-grained after annealing, which is expected and in line with the results in Ref. [40]. However, the coexistence of BCC and FCC phases is observed in all cases, as seen in the XRD records (Fig. 7). Two regions can be observed in the microstructures of all alloys: a dark grey region and a mixed region consisting of alternating light and dark constituents, resembling eutectic. The EDX mapping (Fig. 8) reveals that the mixed region consists of Cu-rich and Fe–Co-rich phases. Chemical compositions of both regions for particular alloys are listed in Table 2 and show that both regions, the dark grey and the mixed, are the same in all alloys, only the ratio between the two regions varies depending on the change in the copper content of the alloys.

In Fig. 9, the HAADF image of the annealed AlCoCu$_{1.5}$FeNi alloy recorded in STEM mode with corresponding STEM-EDX mapping images is shown. Three regions with different compositions can be found in the HAADF image. Region 1 corresponds to the dark grey region in the SEM microstructure, while regions 2 and 3 represent constituents of the mixed region. SAED pattern of region 1 shows that this region consists of a disordered BCC phase. Observation of this region in detail shows that it is inhomogeneous in composition (Fig. 10) with Fe–Co-rich nano-particles inside the Al–Ni-rich matrix, with the Cu content being distributed mainly in the matrix. Similar fine-scale precipitate-like regions rich in Fe and Co in the Al–Ni matrix were already observed in the AlCoFeNi alloy after annealing at 600 °C and subsequent quenching and characterized as the Al–Ni-rich ordered BCC matrix interspersed with fine-scale precipitates of Fe–Co-rich disordered BCC phase [41].

The TEM-EDX mapping in Fig. 9 confirms the SEM results that region 2 is Cu-rich and region 3 is Fe–Co-rich. From both regions, diffraction patterns were taken and chemical compositions were measured (Table 3). According to diffraction patterns, Cu-rich region 2 has a disordered FCC structure, while Fe–Co-rich region 3 has a disordered BCC structure.

To explain the formation of the mixed region, let us look at the
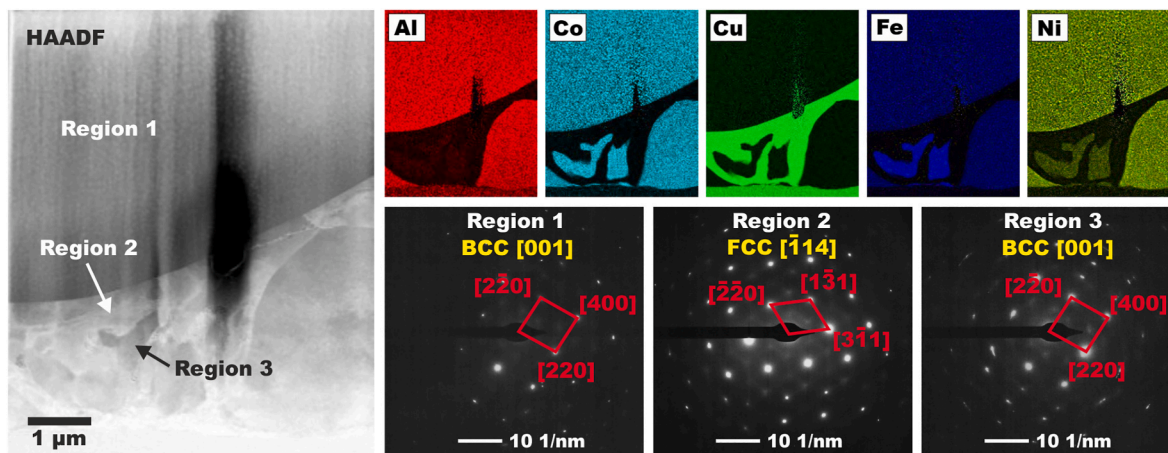
Fig. 9. TEM analysis of the annealed AlCoCu$_{1.5}$FeNi alloy: top right – EDX mapping; left – HAADF image recorded in STEM mode; bottom right – SAED patterns of the three identified distinct regions.
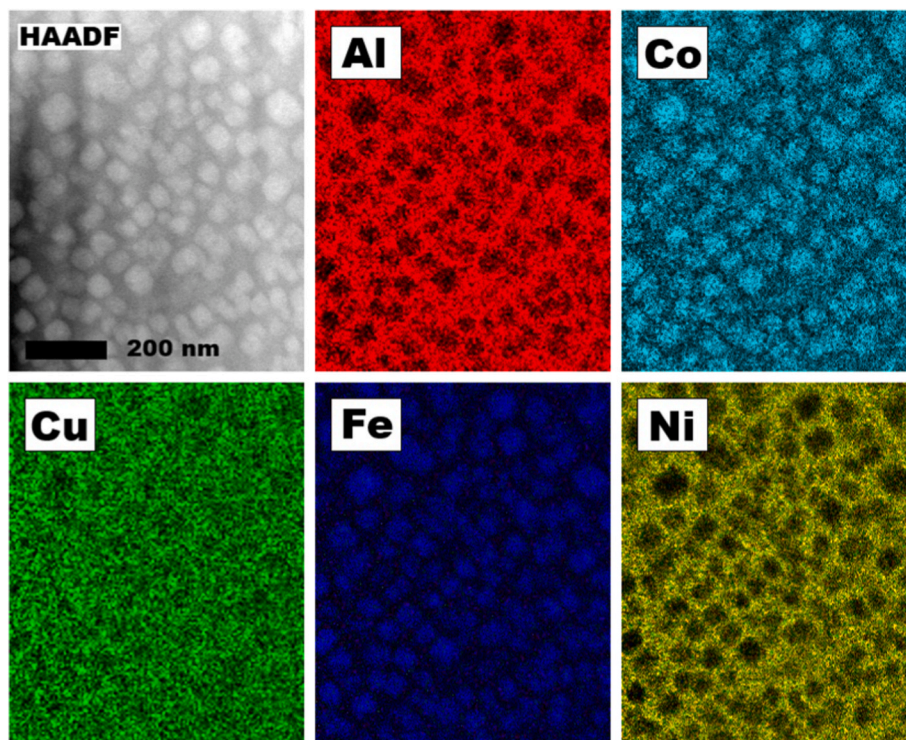

Fig. 10. Detail of the BCC phase of the annealed AlCoCu$_{1.5}$FeNi alloy highlighting Fe–Co-rich nanoparticles inside the Al–Ni-rich matrix: top left – HAADF image; the others – high-resolution EDX mapping of individual elements.

Fe–Co–Cu phase diagram [42]. According to the diagram, the Fe–Co-rich FCC−1 phase occurring at high temperatures and coexisting with the Cu-rich FCC−2 phase changes to the Fe–Co-rich BCC structure as the temperature decreases. Therefore, it can be assumed that the mixed region is formed after annealing from the FCC−1 and FCC−2 phases observed in the as-cast alloys.

Thus, the effect of Cu addition to the AlCoFeNi alloy resides only in the formation of new phases in the microstructure of the alloys but does not affect the phases in terms of order/disorder transformation. That means the ordered BCC and FCC phases, observed after casting, are metastable only and the stable configuration consists of a disordered BCC phase and a mixed region with alternating disordered Fe–Co-rich BCC and Cu-rich FCC phases. In the following section, a possible explanation of this phenomenon is described.

3.3. Order/disorder transformation

A possible reason why ordered structures are formed in all alloys after casting may reside in the strong affinity of Al to bind with most transition metals [28], leading in this way to strong ordering tendencies in both, the BCC and FCC phases. As a result, supercell structures are formed in both phases with sublattices to be occupied by certain elements only. Possible configurations of atoms in such supercell structures are presented in Ref. [34].

After annealing, the microstructure of alloys changed to a more stable configuration, consisting of a disordered BCC phase and the mixed region. As was mentioned, the disordered BCC phase is composed of Fe–Co-rich nanoparticles inside the Al–Ni-rich matrix with Cu distributed mainly in the matrix (Fig. 10). The reason for the formation of such
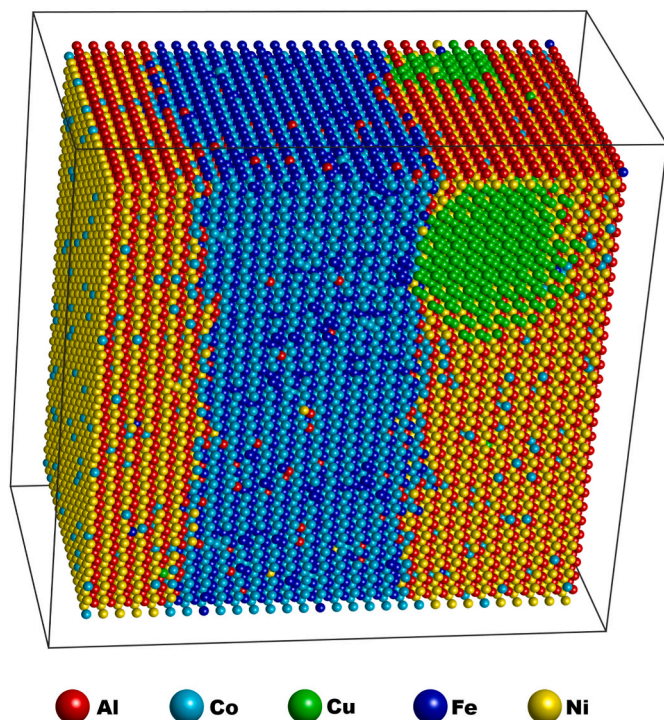
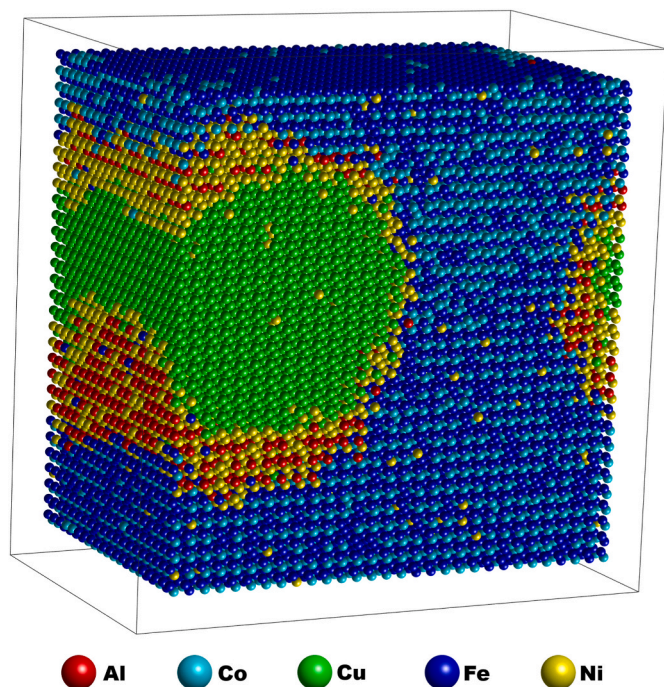**Fig. 11.** A MC simulation snapshot of the equilibrated BCC phase.

Fig. 12. A MC simulation snapshot of the equilibrated BCC phase from the mixed region.

nano-segregated Fe–Co-rich and Al–Ni-rich areas might reside in a reduction of the Gibbs free energy by the interplay between enthalpy and entropy due to the annealing. For a rough estimate of the enthalpy effect on the atomic configuration of the BCC phase, a fixed-lattice Monte Carlo simulation of the BCC lattice was performed using the Bragg-Williams model with pair interatomic interactions based on binary formation enthalpies calculated for the BCC lattice (Table 1). The modelled BCC structure ($30 \times 30 \times 20$ unit cells) with composition

taken as the average composition of the BCC phase after annealing (Table 2) is shown in Fig. 11. As can be seen from Fig. 11, the BCC structure has a tendency to be stable when Al is surrounded mostly by Ni, Fe is surrounded by Co, while Cu is segregated. Thus, when such nanostructures are formed locally, the local enthalpy decreases. A decrease in a local enthalpy leads to a decrease in the total enthalpy of the BCC phase. On the other hand, the random distribution of these nano-segregated regions within a single-phase increases the total configurational entropy of the phase and leads to the uniform distribution of all elements in both sublattices of the BCC phase as a whole. Therefore, the whole phase seems to be disordered, although it may show some degree of ordering at the nanoscale.

The mixed region consists of a Fe–Co-rich BCC phase and almost pure Cu crystallizing in a disordered FCC structure. MC simulation of the BCC phase from the mixed region (Fig. 12) shows that the phase is composed of Cu nanoparticles randomly distributed within the Fe–Co matrix. However, since Cu shows strong immiscibility with Fe and Co [43], both nano-regions must be connected by Al–Ni "bridges". This result simultaneously explains why the Fe–Co-rich BCC phase from the mixed region contains a relatively large amount of Cu (about 20 at. %) in comparison with its counterpart from the Fe–Co–Cu system, where Cu solubility is minimal (about 5 at. %) [42].

4. Conclusions

The addition of Cu to the AlCoFeNi alloy and its effect on the order/disorder behaviour was investigated. The findings can be summarized as follows:

1. Increasing Cu ratio in the AlCoCu$_x$FeNi leads to a gradual transition from virtually pure BCC structure for $x = 0.6$ to pure FCC for $x = 3.0$ in the as-cast state, as expected. However, the system contains not only one FCC phase but at least at higher Cu concentration it is composed of two FCC phases, Fe–Co-rich dendritic (FCC-1) and Cu-rich interdendritic (FCC-2) with very close lattice parameters. All observed phases are ordered.
2. After annealing, the microstructure consists of disordered phases and it is composed of a BCC phase, containing Fe–Co-rich nanoparticles inside the Al–Ni-rich matrix, and a mixed region, consisting of a BCC phase intergrown with Cu-rich FCC phase. The ratio between the BCC phase and the mixed region also follows the Cu content. The reason for the formation of nanostructures inside the BCC phase might reside in a reduction of the Gibbs free energy by the interplay between enthalpy and entropy due to the annealing.
3. The formation of ordered structures in the as-cast state is explained by the strong affinity of Al to transition metals, which in all phases results in the formation of supercell structures having sublattices occupied by certain elements only.
4. Disordered structures after annealing are formed for two reasons. The FCC phase is composed of nearly pure Cu which is disordered by default. The BCC phases are composed of randomly distributed nano-segregated regions within a single-phase resulting in a uniform distribution of all elements in both sublattices of the BCC phase, which therefore seems to be macroscopically disordered, although it may show some degree of ordering at the nanoscale.

CRediT author statement

P. Priputen: Conceptualization, Supervision, Formal analysis, Writing - Original Draft, Funding acquisition; **P. Noga:** Writing - Review & Editing, Funding acquisition; **M. Novaković:** Investigation, Formal analysis, Funding acquisition; **J. Potočnik:** Investigation, Formal analysis; **A. Antušek:** Methodology, Software; **R. Bujdák:** Software; **E. Bachleda:** Investigation; **M. Drienovský:** Methodology; **M. Nosko:** Resources.

Declaration of competing interest

The authors declare that they have no known competing financial interests or personal relationships that could have appeared to influence the work reported in this paper.

Data availability

Data will be made available on request.

Acknowledgement

References

[1] M.H. Tsai, J.W. Yeh, High-entropy alloys: a critical review, Mater. Res. Lett. 2 (2014) 107–123, https://doi.org/10.1080/21663831.2014.912690.

[2] Y. Zhang, T.T. Zuo, Z. Tang, M.C. Gao, K.A. Dahmen, P.K. Liaw, Z.P. Lu, Microstructures and properties of high-entropy alloys, Prog. Mater. Sci. 61 (2014) 1–93, https://doi.org/10.1016/j.pmatsci.2013.10.001.

[3] Y.F. Ye, Q. Wang, J. Lu, C.T. Liu, Y. Yang, High-entropy alloys: challenges and prospects, Mater. Today 19 (2016) 349–362, https://doi.org/10.1016/j.mattod.2015.11.026.

[4] D.B. Miracle, O.N. Senkov, A critical review of high entropy alloys and related concepts, Acta Mater. 122 (2017) 448–511, https://doi.org/10.1016/j.actamat.2016.08.081.

[5] Y.-F. Kao, S.-K. Chen, T.-J. Chen, P.-C. Chu, J.-W. Yeh, S.-J. Lin, Electrical, magnetic, and Hall properties of AlxCoCrFeNi high-entropy alloys, J. Alloys Compd. 509 (2011) 1607–1614, https://doi.org/10.1016/j.jallcom.2010.10.210.

[6] M.S. Lucas, L. Mauger, J.A. Muñoz, Y. Xiao, A.O. Sheets, S.L. Semiatin, J. Horwath, Z. Turgut, Magnetic and vibrational properties of high-entropy alloys, J. Appl. Phys. 109 (2011), 07E307, https://doi.org/10.1063/1.3538936.

[7] Y. Zhang, T. Zuo, Y. Cheng, P.K. Liaw, High-entropy alloys with high saturation magnetization, electrical resistivity, and malleability, Sci. Rep. 3 (2013) 1455, https://doi.org/10.1038/srep01455.

[8] F. Körmann, D. Ma, D.D. Belyea, M.S. Lucas, C.W. Miller, B. Grabowski, M.H. F. Sluiter, "Treasure maps" for magnetic high-entropy-alloys from theory and experiment, Appl. Phys. Lett. 107 (2015), 142404, https://doi.org/10.1063/1.4932571.

[9] Z. Li, K.G. Pradeep, Y. Deng, D. Raabe, C.C. Tasan, Metastable high-entropy dual-phase alloys overcome the strength–ductility trade-off, Nature 534 (2016) 227–230, https://doi.org/10.1038/nature17981.

[10] C. Niu, C.R. LaRosa, J. Miao, M.J. Mills, M. Ghazisaeidi, Magnetically-driven phase transformation strengthening in high entropy alloys, Nat. Commun. 9 (2018) 1–9, https://doi.org/10.1038/s41467-018-03846-0.

[11] J.-W. Yeh, S.-K. Chen, S.-J. Lin, J.-Y. Gan, T.-S. Chin, T.-T. Shun, C.-H. Tsau, S.-Y. Chang, Nanostructured high-entropy alloys with multiple principal elements: novel alloy design concepts and outcomes, Adv. Eng. Mater. 6 (2004) 299–303, https://doi.org/10.1002/adem.200300567.

[12] J.W. Yeh, Recent progress in high-entropy alloys, Ann. Chim. Sci. Mater. 31 (2006) 633–648.

[13] E.J. Pickering, N.G. Jones, High-entropy alloys: a critical assessment of their founding principles and future prospects, Int. Mater. Rev. 61 (2016) 183–202, https://doi.org/10.1080/09506608.2016.1180020.

[14] E.P. George, D. Raabe, R.O. Ritchie, High-entropy alloys, Nat. Rev. Mater. 4 (2019) 515–534, https://doi.org/10.1038/s41578-019-0121-4.

[15] X. Chang, M. Zeng, K. Liu, L. Fu, Phase engineering of high-entropy alloys, Adv. Mater. 32 (2020), 1907226, https://doi.org/10.1002/adma.201907226.

[16] S.A. Kube, S. Sohn, D. Uhl, A. Datye, A. Mehta, J. Schroers, Phase selection motifs in High Entropy Alloys revealed through combinatorial methods: large atomic size difference favors BCC over FCC, Acta Mater. 166 (2019) 677–686, https://doi.org/10.1016/j.actamat.2019.01.023.

[17] Y. Ikeda, B. Grabowski, F. Körmann, Ab initio phase stabilities and mechanical properties of multicomponent alloys: a comprehensive review for high entropy alloys and compositionally complex alloys, Mater. Char. 147 (2019) 464–511, https://doi.org/10.1016/j.matchar.2018.06.019.

[18] M. Laurent-Brocq, L. Perrière, R. Pirès, Y. Champion, From high entropy alloys to diluted multi-component alloys: range of existence of a solid-solution, Mater. Des. 103 (2016) 84–89, https://doi.org/10.1016/j.matdes.2016.04.046.

[19] S. Gorsse, D.B. Miracle, O.N. Senkov, Mapping the world of complex concentrated alloys, Acta Mater. 135 (2017) 177–187, https://doi.org/10.1016/j.actamat.2017.06.027.

[20] S. Gorsse, J.-P. Couzinié, D.B. Miracle, From high-entropy alloys to complex concentrated alloys, C. R. Phys. 19 (2018) 721–736, https://doi.org/10.1016/j.crhy.2018.09.004.

[21] A.M. Manzoni, U. Glatzel, New multiphase compositionally complex alloys driven by the high entropy alloy approach, Mater. Char. 147 (2019) 512–532, https://doi.org/10.1016/j.matchar.2018.06.036.

[22] V.K. Pandey, Y. Shadangi, V. Shivam, B.N. Sarma, N.K. Mukhopadhyay, Theoretical and experimental study on phase stability of TiVZrMoW refractory high entropy alloy, Philos. Mag. A 102 (2022) 480–503, https://doi.org/10.1080/14786435.2021.2001066.

[23] R. Kulkarni, B.S. Murty, V. Srinivas, Study of microstructure and magnetic properties of AlNiCo(CuFe) high entropy alloy, J. Alloys Compd. 746 (2018) 194–199, https://doi.org/10.1016/j.jallcom.2018.02.275.

[24] D.P. Landau, K. Binder, A Guide to Monte Carlo Simulations in Statistical Physics, fourth ed., Cambridge University Press, 2014.

[25] W.L. Bragg, E.J. Williams, The effect of thermal agitation on atomic arrangement in alloys, P. Roy. Soc. A-Math. Phy. 145 (1934) 699–730, https://doi.org/10.1098/rspa.1934.0132.

[26] J.P. Perdew, K. Burke, M. Ernzerhof, Generalized gradient approximation made simple, Phys. Rev. Lett. 77 (1996) 3865–3868, https://doi.org/10.1103/PhysRevLett.77.3865.

[27] D. Vanderbilt, Soft self-consistent pseudopotentials in a generalized eigenvalue formalism, Phys. Rev. B 41 (1990) 7892–7895, https://doi.org/10.1103/PhysRevB.41.7892.

[28] L.J. Santodonato, P.K. Liaw, R.R. Unocic, H. Bei, J.R. Morris, Predictive multiphase evolution in Al-containing high-entropy alloys, Nat. Commun. 9 (2018) 4520, https://doi.org/10.1038/s41467-018-06757-2.

[29] D. Frenkel, B. Smit, Understanding Molecular Simulation: from Algorithms to Applications, second ed., Academic Press, San Diego, 2001.

[30] Y.X. Zhuang, W.J. Liu, P.F. Xing, F. Wang, J.C. He, Effect of Co element on microstructure and mechanical properties of FeCoxNiCuAl alloys, Acta Metall. Sin. 25 (2012) 124–130, https://doi.org/10.11890/1006-7191-122-124.

[31] Y.X. Zhuang, W.J. Liu, Z.Y. Chen, H.D. Xue, J.C. He, Effect of elemental interaction on microstructure and mechanical properties of FeCoNiCuAl alloys, Mater. Sci. Eng. A. 556 (2012) 395–399, https://doi.org/10.1016/j.msea.2012.07.003.

[32] N.A. Krapivka, S.A. Firstov, M.V. Karpets, A.N. Myslivchenko, V.F. Gorban', Features of phase and structure formation in high-entropy alloys of the AlCrFeCoNiCux system (x = 0, 0.5, 1.0, 2.0, 3.0), Phys. Met. Metallogr. 116 (2015) 467–474, https://doi.org/10.1134/S0031918X15030084.

[33] V.P. Vorob'eva, A.E. Zelenaya, V.I. Lutsyk, S.I. Sineva, R.V. Starykh, O. S. Novozhilova, High-temperature area of the Fe-Ni-Co-Cu phase diagram: experimental study and computer design, J. Phase Equilibria Diffus. 42 (2021) 175–193, https://doi.org/10.1007/s11669-021-00863-3.

[34] M. Beyramali Kivy, M. Asle Zaeem, S. Lekakh, Investigating phase formations in cast AlFeCoNiCu high entropy alloys by combination of computational modeling and experiments, Mater. Des. 127 (2017) 224–232, https://doi.org/10.1016/j.matdes.2017.04.086.

[35] M. Zhang, X. Zhou, D. Wang, W. Zhu, J. Li, Y.F. Zhao, AlCoCuFeNi high-entropy alloy with tailored microstructure and outstanding compressive properties fabricated via selective laser melting with heat treatment, Mater. Sci. Eng. A 743 (2019) 773–784, https://doi.org/10.1016/j.msea.2018.11.118.

[36] V. Shivam, S. Kar, G.K. Bansal, A.K. Chandan, B.K. Sahoo, G.K. Mandal, N. K. Mukhopadhyay, V.C. Srivastava, A novel Fe-rich non-equiatomic medium-entropy alloy with superior mechanical properties, J. Alloys Compd. 952 (2023), 170029, https://doi.org/10.1016/j.jallcom.2023.170029.

[37] V. Shivam, J. Basu, R. Manna, N.K. Mukhopadhyay, Local composition migration induced microstructural evolution and mechanical properties of non-equiatomic Fe40Cr25Ni15 Al15Co5 medium-entropy alloy, Metall. Mater. Trans. A. 52 (2021) 1777–1789, https://doi.org/10.1007/s11661-021-06188-7.

[38] H. Jain, Y. Shadangi, D. Chakravarty, K. Chattopadhyay, A.K. Dubey, N. K. Mukhopadhyay, Low-density Fe40Mn19Ni15Al15Si10C1 high entropy steel processed by mechanical alloying and spark plasma sintering: phase evolution, microstructure and mechanical properties, Mater. Sci. Eng., A 869 (2023), 144776, https://doi.org/10.1016/j.msea.2023.144776.

[39] P.F. Yu, H. Cheng, L.J. Zhang, H. Zhang, M.Z. Ma, G. Li, P.K. Liaw, R.P. Liu, Nanotwin's formation and growth in an AlCoCuFeNi high-entropy alloy, Scripta Mater. 114 (2016) 31–34, https://doi.org/10.1016/j.scriptamat.2015.11.032.

[40] Y.X. Zhuang, H.D. Xue, Z.Y. Chen, Z.Y. Hu, J.C. He, Effect of annealing treatment on microstructures and mechanical properties of FeCoNiCuAl high entropy alloys, Mater. Sci. Eng. A. 572 (2013) 30–35, https://doi.org/10.1016/j.msea.2013.01.081.

[41] V. Chaudhary, B. Gwalani, V. Soni, R.V. Ramanujan, R. Banerjee, Influence of Cr substitution and temperature on hierarchical phase decomposition in the AlCoFeNi high entropy alloy, Sci. Rep. 8 (2018), 15578, https://doi.org/10.1038/s41598-018-33922-w.

[42] M. Palumbo, S. Curiotto, L. Battezzati, Thermodynamic analysis of the stable and metastable Co–Cu and Co–Cu–Fe phase diagrams, Calphad 30 (2006) 171–178, https://doi.org/10.1016/j.calphad.2005.10.007.

[43] Y. Nakagawa, Liquid immiscibility in copper-iron and copper-cobalt systems in the supercooled state, Acta Mater. 6 (1958) 704–711, https://doi.org/10.1016/0001-6160(58)90061-0.